Yuri V. Vassilevski, Alexander A. Danilov, Timur M. Gamilov, Yuri A. Ivanov, Roman A. Pryamonosov, and Sergey S. Simakov

Patient-specific anatomical models in human physiology

Abstract: Patient-specific simulations of human physiological processes remain the challenge for many years. Detailed 3D reconstruction of body anatomical parts on the basis of medical images is an important stage of individualized simulations in physiology. In this paper we present and develop the methods and algorithms for construction of patient-specific discrete geometric models. These models are represented by anatomically correct computational meshes. Practical use of these methods is demonstrated for two important medical applications: numerical evaluation of fractional flow reserve in coronary arteries and electrocardiography simulation.

Keywords: Medical image processing, mathematical modelling, fractional flow reserve, coronary circulation, electrocardiography, patient-specific modelling.

MSC 2010: 68U10, 92C55, 76Z05

DOI: 10.1515/rnam-2015-0017
Received April 10, 2015; accepted April 14, 2015

Individualized numerical simulations of physiological processes in the human body remain the challenge for many years. Contemporary resolution of medical images and new algorithms for their postprocessing allow to develop anatomically correct numerical models of various processes such as patient-specific blood circulation, cardiac electrophysiology etc. In this paper we present and develop the methods and algorithms for construction of patient-specific discrete geometric models. These models are represented by anatomically correct computational meshes. The methods are general-purpose and can be applied to any region or network of the human body. We demonstrate practicability of the methods for two important medical applications. Each application imposes specific restrictions on both the input medical images and the output patient-specific discrete model, and, therefore, calls for a specific class of 3D reconstruction methods. The first application deals with numerical evaluation of fractional flow reserve (FFR) in coronary arteries. The second application deals with electrocardiography simulation (ECG).

Atherosclerotic diseases of coronary vessels are the main reasons of widespread myocardial ischemia frequently resulting in disability or death. The basic methods of medical treatment assume invasive endovascular intervention (bypassing, stenting, et al.). The use of these methods is restricted in some cases due to personal contraindications or low effectiveness. The main criterion of the endovascular surgical treatment efficiency is the value of FFR. It is calculated as the ratio of the mean coronary pressure distal to the lesion after dilator administration to the mean aortic pressure [20, 27, 52]. The coronary pressure is normally measured by ultrasound endovascular transducer. This measurement requires expensive and invasive endovascular intervention. Contemporary non-invasive methods are based on 3D blood flow simulation in the vicinity of the lesion [20]. The method is subject to criticism [34, 50] due to bad posedness of upstream and downstream boundary conditions, rigid wall approximation for the vessel tissue, large computational cost, general difficulties in parameters fitting.

Yuri V. Vassilevski, Alexander A. Danilov, Sergey S. Simakov: Institute of Numerical Mathematics of the RAS, Moscow 119333, Russia
Yuri V. Vassilevski, Alexander A. Danilov, Timur M. Gamilov, Yuri A. Ivanov, Roman A. Pryamonosov, Sergey S. Simakov: Moscow Institute of Physics and Technology, Dolgoprudny 141700, Moscow region, Russia
Yuri V. Vassilevski, Roman A. Pryamonosov: M. V. Lomonosov Moscow State University, Moscow 119991, Russia
Sergey S. Simakov: Institute of Computer Aided Design of the RAS, Moscow 123056, Russia

In this work we present the new numerical technique for non-invasive numerical estimate of FFR on the basis of computed tomography (CT) data. The estimate is based on 1D blood flow modelling in vascular networks and reconstruction of patient-specific coronary network. We show that FFR value depends on the heart ejection intensity. Since clinical measurements are available in quiet conditions only, FFR under intensive heart rates can be estimated only numerically. This observation gives the additional motivation for the technology of individual virtual FFR assessment.

Our approach to the numerical estimate of FFR is based on coupling patient-specific coronary flow simulation and physiologically correct simulation of the blood flow in a reference cardiovascular system. The corner stone of the approach is automatic construction of a global anatomically correct 1D computational graph adapted to patient coronary network. Individualized regional network of coronary vessels is built from patient-specific CT-scans by our fully automatic algorithm for coronary arteries identification. It starts from the fast variant of the isoperimetric distance trees algorithm [15] for aorta identification. The coronary network is reconstructed by the use of the Frangi vesselness filter [9]. The filter is based on the Hessian 3D analysis of the CT-image and is applicable for all tubular structures in the vascular data set. A global 3D vascular network (1D computational graph) of the systemic circulation is built on the basis of the anatomically correct database [55] by the automatic algorithm [12]. The regional and the global networks are merged by our adaptation algorithm performing the similarity function analysis (see Section 1.3.2). The algorithm is a specific realization of a general approach whose detailed description and applications are given in [4]. The other parameters of our model of blood flows in 1D vascular networks are obtained as follows. Elastic properties of the blood vessels are adjusted to typical values from clinical studies [1, 36] categorized according to age, physical conditions, etc. Hydraulic resistance coefficients are adjusted by fitting model linear velocity to individual ultrasound measurements similar to our previous works [12, 38].

Electrocardiogram is the well known graphical representation of the cardiac electrical function. It is recorded during ECG procedure, a non-invasive medical procedure of measuring electric potential activity on the body surface. In clinical practice ECG is widely used in medical examination as the early non-invasive detection of heart disease. The four limb electrode electrocardiograms have been used for decades, and ECG modelling highly improved comprehension of this process. Recently the computer algorithms become used for dispersion analysis of low amplitude ECG signal oscillations producing highly sensitive analysis of the re-polarization phase, the most challenging phase of heart excitement in clinical interpretation [19].

The modelling of cardiac electrophysiology may be formalized as the full-scale study of the heart electrical activity from inner-cellular level to the electrode recordings at the body surface. Various mathematical models and numerical methods have been developed for modelling of cardiac electrophysiology [24]. Generally the full-scale ECG modelling involves simulations of electric potential propagation on three different scales: the single-cell models represented by ODE are used on the cellular level, the bidomain model represented by PDE system is used on the cardiac tissue level, the simplified quasi-static version of Maxwell's equations is used on the whole-body level. Recently the pipeline for verification of electrophysiology solvers was proposed [28]. Other validation techniques were discussed in [21].

The mathematical models of ECG may be used to estimate impacts of various processes on the electrocardiogram [53] and to evaluate how different cardiac pathologies may affect ECG readings. Our future work is aimed at modelling ECG for patients with congenital heart disease. The reconstruction of personalized anatomical model of the pathological heart is one of the crucial steps in ECG modelling. The bidomain model requires an accurate anatomical model of patient heart accounting the myocardial anisotropy structure. The magnetic resonance imaging (MRI) may be used to obtain both the anatomical structure of the heart and the anisotropy structure of the cardiac tissue. Accurate patient-specific anatomical reconstruction of torso requires the high resolution medical imaging data like CT or MRI for the whole body, which in most cases is not available. However, the anthropometric measurements of the patient's body are easily accessible, and thorax CT/MRI images may be used to construct subject specific patient' thorax anatomical model. Our preliminary simulations indicate that ECG readings have low sensitivity to segmentation errors outside the thorax region. Thus, patient-specific segmentation should be focused on the cardiac region, and a reference human model may be used in the remaining part of the body. Using this concept we investigate the impact of the anatomical

structure in the thorax region on ECG reading. Our preliminary ECG simulation uses decoupled monodomain equation for the cardiac tissue and Laplace equation for the torso region.

The corner stone for medical image processing is a segmentation process when each voxel of the 3D medical image is assigned with the particular tissue or internal organ. Various medical image segmentation techniques have been developed [17, 33, 49]. The most promising fully automatic segmentation methods belong to atlas-based segmentation techniques. The patient-specific segmentation is obtained from the atlas of presegmented images of other individuals. This atlas should contain enough different cases for accurate mapping of the new patient data. Thus atlas-based approach requires huge amount of segmentation expert work for the preparation of atlases and development of algorithms dealing with big data. Semi-automatic segmentation technologies require interaction with the expert. They are used primarily for precise local segmentations, where only one organ or tissue is processed. In this work we use our technique for adaptation of the once segmented reference human model to different individuals. This technique relies on anthropometric scaling, control points mapping and supervised segmentation [7].

The paper outline is as follows. In Section 1 we discuss and present several methods for 3D reconstruction of patient body from medical images. In particular, we consider segmentation of medical images for the whole body and its vascular network, as well as our approaches to patient-specific adaptation of reference models. In Section 2 we demonstrate the use of the patient-specific reconstruction for two medical applications, the numerical estimate of FFR and the numerical simulation in cardiac electrophysiology.

1 3D reconstruction of patient body from medical images

1.1 Sources of medical images

The anatomical 3D data are usually provided in the form of medical image data sets (scans) from imaging modalities such as computed tomography (CT) and magnetic resonance imaging (MRI). The MRI intensity is sensitive to the molecular dynamics of tissue water. The random rotational motion of water molecules provides intrinsic 'relaxation' properties relating to the rate by which the excitable MRI signal recovers (referred to as T1) or the excited signal decays (T2). Special modality study can be used for better resolution of particular tissues. For instance, accurate blood vessel geometry reconstruction is obtained by contrast imaging. High contrast vessel images can be gained from contrast-enhanced magnetic resonance angiography (ceMRA) or contrast-enhanced computed tomography angiography (CTA). In several physiological models the tissue structure should be defined. Anisotropic structure of cardiac tissue is recovered by the magnetic resonance diffusion tensor imaging (MR-DTI) [18], a subset of MRI that measures the anisotropy of water diffusion induced when tissues have an ordered organization. Different modalities exhibit differently in visualization of specific tissues, and therefore various protocols are used to capture specific properties of patient body. Usually, regardless of the protocol, imaging data are represented by scalar, vector or tensor volumetric arrays in DICOM format.

All the above imaging modalities are patient-specific and non-invasive. Invasive study such as histology is more accurate and less comfortable: it requires sampling, fixation, mounting, and microscopic examination of the tissue. Histology studies are patient-specific and allow to recover anisotropic structure of the tissues. We also mention the Visible Human Project (VHP) [56] directed to complete, anatomically detailed 3D representations of the normal male and female human bodies. For that purpose transverse CT, MRI and cryosection images of representative male and female cadavers were obtained. These data sets provide detailed information on the human anatomic structure, they may be used for the preparation of a reference anatomical model.

1.2 Medical image processing

A discrete anatomical model can be obtained from medical images or from custom 3D geometric models. Medical images are personalized data whereas custom 3D geometric models are reference, or averaged, data.

An anatomically accurate geometric 3D model of a body or its part represents organs and tissues as 3D subdomains with given boundaries. Geometric models are designed for the study of anatomy via 3D visualization and therefore can provide medical images. An example of a geometric model is the Plastic Boy model [55]. A geometric model can serve as the basis for the construction of a reference discrete model of a body or its parts. The reference discrete model can be further adapted for patient body or its parts, see Section 1.3. For instance, in Section 1.3.2 we consider a graph representation of a reference vascular network [12] extracted from the geometric database [55]. The reference graph can be adapted regionally to individual data by specific black-box algorithms. We note that 3D geometric models of internal body structures can hardly be used in simulations without tedious preprocessing. Indeed, the model should provide the desired level of specification, it should be anatomically correct: the internal tissues and organs should not intersect, and there should not exist void regions between the tissues inside the body.

In the remaining part of this section we consider the methods for generation of a discrete anatomical model from patient-specific medical images. The first stage of medical image processing is image segmentation. In segmented image the set of voxels with the same label represents the specific tissue. Since all voxels are labeled with unique tissue labels, the segmented tissues do not intersect and do not leave void regions inside the body. The segmented volume array can serve as a patient-specific geometric model. Also, it provides all necessary information for generation of a discrete anatomical model: in Section 1.2.1 we discuss generation of a 3D computational mesh for a whole body, in Section 1.2.2 we discuss generation of a 1D computational graph for a vascular network.

1.2.1 Full body reconstruction

We used Visible Human Project (VHP) [56] data to construct the discrete full body model. The initial segmentation was performed for the torso region of the human body [7]. The original volume array of the human torso was derived from the male data. The initial segmented model of the VHP man torso is an array of 567×305×843 colored voxels with the 1×1×1 mm resolution [16]. This model has been produced primarily for visualization purposes and contained a significant amount of unclassified tissues. We performed further semi-automatic processing of the whole body using ITK-SNAP segmentation software program [51]. At the final stage, we used several post-processing algorithms for filling the gaps between tissues and final segmented data smoothing. The obtained segmented model contains 32 materials and effective resolution of 1 mm [7]. Similar anatomical model is also constructed for the VHP female data set.

The segmented image may be treated as a 3D array of integers. Each value is associated with certain material. Correct resolution of small scale structures may require improvement of input data resolution. This is achieved by splitting the initial multi-labeled segmented array into several binary layers associated with distinct materials. Image upscaling and smoothing operators are applied to each material layer separately. As the result, the binary data may become rational values. The material layers are assembled to the joint multi-labeled segmented image by assigning to each voxel the material whose layer has the largest rational value at this location.

A computational mesh may be generated by several methods, including marching cubes algorithm for surface reconstruction [47], surface triangulation smoothing and coarsening [41, 46], 3D Delaunay triangulation [10], and advancing front technique for volume mesh generation [5, 10]. We suggest using the Delaunay triangulation algorithm from the CGAL-Mesh library [35]. This algorithm enables defining a specific mesh size for each model material. In order to preserve geometric features of the segmented model while keeping the number of vertices feasible, we assign a smaller mesh size to blood vessels and a larger mesh size to fat and muscle tissues. An example of unstructured grid with high adaptation to heart ventricles is presented in Fig. 1. An optional skin layer may be added to the surface of the constructed mesh. The boundary triangulation is

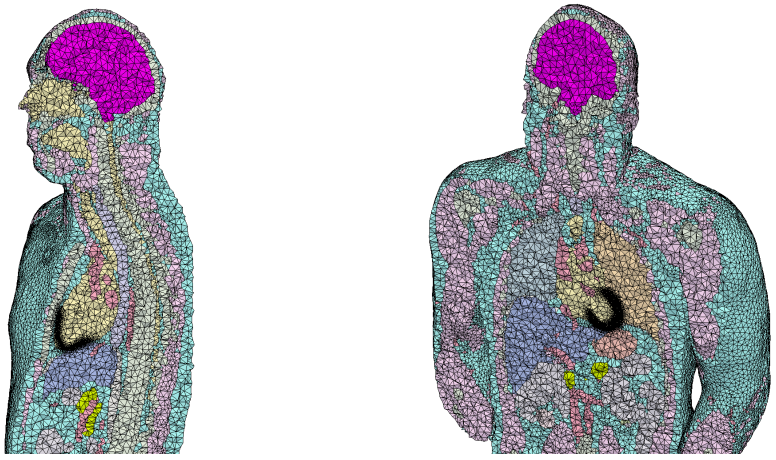

(a) (b)

Figure 1. Unstructured tetrahedral mesh for VHP reference model with aggressive adaptation to heart ventricles, 2049945 tetrahedra, 370242 vertices: (a) sagittal cross-section, (b) coronal cross-section.

used to create a prismatic mesh on the surface, and then each prism is split into three tetrahedra resulting in a conformal mesh. Mesh cosmetics algorithms from the Ani3D library [54] are used to improve mesh quality. This essential step reduces the error of the finite element discretization and the condition number of the resulted matrices.

1.2.2 Vascular network reconstruction

The vascular network is a 3D tubular structure composed of vessels and their bifurcations (junctions). In this section we discuss how the discrete model (1D computational graph) of the vascular network can be constructed. In ceMRA/CTA data appropriate voxels are characterized by high brightness. Automatic segmentation methods exploit the basic geometric feature of network vessels, a tube-like structure, which can be detected by the image Hessian analysis. The most powerful and anatomically correct method is the Frangi vesselness filter [9]: it is applicable even for discontinuous structures which are produced by the moving vessels such as coronary arteries. The alternative centerline tracking method [22] combines series of fast local 2D Hessian eigenanalysis in vessels and series of fast local 3D Hessian eigenanalysis in bifurcations. The local analyses provide much faster performance compared to the global 3D Frangi filter and thus are applicable to automatic segmentation of extensive networks in large data sets. We shall address both methods and present their application to segmentation, skeletonization and centerline tracking of coronary and main leg arteries yielding 1D computational graphs of these regional networks.

The Frangi filter measures similarity of a 3D object to a tubular structure with the Hessian eigenanalysis. The method refers to a measurement scale associated with a certain range of vessel diameter. Let an image be given as a function of coordinates $\mathbf{x}$ and its Hessian matrix $\mathcal{H}_\sigma(\mathbf{x}_0)$ be computed at scale σ at point $\mathbf{x}_0$ in accordance with the linear scale space theory [8]. Let $|\lambda_1| \le |\lambda_2| \le |\lambda_3|$ be moduli of eigenvalues and $\mathbf{v}_1, \mathbf{v}_2, \mathbf{v}_3$ be eigenvectors of $\mathcal{H}_\sigma(\mathbf{x}_0)$. The Frangi filter of bright tubular structures is based on the following Hessian features:

$$|\lambda_1| \approx 0, \qquad |\lambda_1| \ll |\lambda_2|, \qquad \lambda_2 \approx \lambda_3 < 0$$

the eigenvector $\mathbf{v}_1$ indicates the direction along the tube with approximate radius σ, whereas the eigenvectors $\mathbf{v}_2, \mathbf{v}_3$ span the cross-section of the tube. Frangi defined the line vesselness measure $V_\sigma(\mathbf{x}_0) = V_\sigma(\mathbf{x}_0, \lambda_1, \lambda_2, \lambda_3, \alpha, \beta, c)$ associated to the scale σ. Parameters α, β, c are thresholds controlling sensitivity [9] of the line filter to the Frangi measures. The scale σ allows to identify vessels whose radius is approxi-

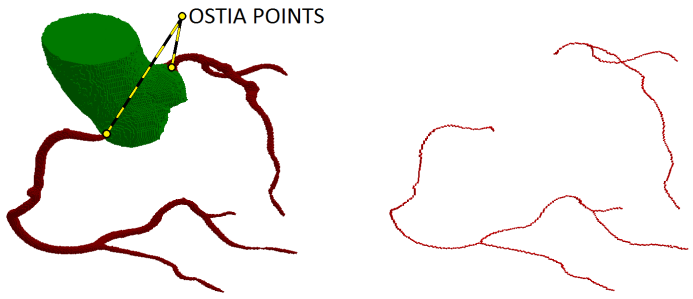

Figure 2. Segmentation of coronary arteries, CT data with resolution 512x512x401: (a) aorta is segmented with IDT-based algorithm and coronary arteries are segmented with the Frangi filter, (b) skeletonized coronary network.

mately equal to σ. The multiscale Frangi filter is computed in range of scales $\sigma_{\min} \le \sigma \le \sigma_{\max}$ to identify the vessels of all sizes:

$$V_{\text{mult}}(\mathbf{x}_0) = \max_{\sigma_{\min} \le \sigma \le \sigma_{\max}} V_\sigma(\mathbf{x}_0).$$

The Frangi filter is a computationally costly procedure. For large data sets with a large variety of vessel diameters it can be very expensive, although for regional vascular networks it is robust and efficient. For instance, segmentation of coronary arteries by the vesselness filter takes less than 3 minutes on PC for CT data sets with 512×512×401 voxels, the segmented vessels are presented in Fig. 2a.

With the use of the Frangi filter we developed an automated technology [4] for segmentation of coronary arteries. Similar to [42, 48], the technological chain consists of three stages: aorta segmentation, ostia points detection and segmentation of coronary arteries. The aorta segmentation algorithm is based on the Isoperimetric Distance Trees (IDT) method [15] and works only with a mask (masked voxels). The algorithm initializes the mask containing the aorta, cuts the initial mask at bottlenecks, smooths and denoises the final submask. For details we refer to [4]. The next stage is Frangi filtering with the parameters $\alpha = 0.5$, $\beta = 0.5$, $c = 500$ at three scales $\sigma = 1, 2, 3$. Ostia points are detected as two distinct local maxima of Frangi vesselness inside the aorta mask. The coronary arteries are defined as components of vascular trees rooting at ostia points, see Fig. 2a. From segmented arteries we extract centerlines by the use of skeletonization and specific denoising algorithms [4]. The final skeleton (coronary centerlines) is shown in Fig. 2b.

Another approach, the centerline tracking is based on the local structure analysis algorithm [22]. The algorithm can provide either segmentation or centerlines (a sequence of seeds and associated radii) without segmentation. The algorithm reduces the problem of identification of a tubular structure to a sequence of identifications of its cross-sections ordered along the tube centerline. The above trunk analysis is applicable between bifurcations of vessels, trunk segmentation being amenable via thresholding in each cross-section. In bifurcation region a 3D Hessian-based bifurcation filter is to be applied. The bifurcation analysis inputs a bifurcation cross-section of already identified vessel and outputs initial seeds for two other uninitialized vessels. The algorithm can not identify junctions of more than 3 vessels and junctions of vessels with large ratio of diameters.

In order to start trunk analysis, we need an initial seed, direction and approximate radius r_0. The local 3D Hessian eigendecomposition at scale r_0 gives a cross-section plane at the seed spanned by the eigenvectors $\mathbf{v}_2$ and $\mathbf{v}_3$. By using the Canny edge filter we detect the vessel border and the local adaptive threshold which can be used for trunk segmentation. Since the initial seed is only an approximation of the center of vessel cross-section, we correct the seed coordinates by the use of 2D Hessian analysis [22]. To adjust the vessel radius r_p, one computes the diameters d_2 and d_3 of the vessel along the vectors $\mathbf{v}_2$ and $\mathbf{v}_3$, respectively, and sets $r_p = (d_2 + d_3)/4$. The initial seed for the next cross-section is found by shifting the current seed along the vessel direction $\mathbf{v}_1$ as shown in Fig.3a.

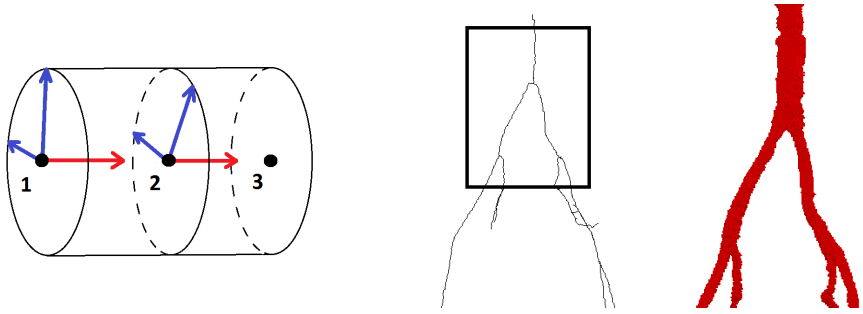

(a) (b) (c)

Figure 3. Centerline tracking: (a) trunk analysis: blue vectors span tube cross-sections, red vectors direct along the tube, (b) an example of extracted centerlines for leg arteries, (c) vessel segmentation in region that is restricted by the rectangle in (b).

The refinement of seed coordinates is based on the circleness enhancement ratio

$$C_R(\mathbf{x}) = \frac{|\lambda_{2D,1}(\mathbf{x}) + \lambda_{2D,2}(\mathbf{x})|}{|\lambda_{2D,2}(\mathbf{x})| - |\lambda_{2D,1}(\mathbf{x})|}$$

attaining its maximum at the center of the cross-section. To account the noisy nature of medical images, we define the circleness function as follows:

$$C(\mathbf{x}) = \left(1 - \mathrm{e}^{-(C_R(\mathbf{x})\alpha)^2}\right)\left(1 - \mathrm{e}^{-(\lambda_{2D,1}^2(\mathbf{x})+\lambda_{2D,2}^2(\mathbf{x}))/(2\beta^2)}\right).$$

Here α controls the increase rate of the width of the Gaussian profile of circleness C, and β regulates the effect of noise. The refined seed coordinates correspond to the maximum of circleness C in the cross-section.

The trunk analysis stops when the cross-section intersects a bifurcation or if the new initial seed falls outside the vessel (i.e. $\lambda_2 \geq 0$ or $\lambda_3 \geq 0$). The latter means termination of the vessel due to insufficient CT resolution. The criterion for the bifurcation intersection is a prolate shape of the vessel cross-section. For typical arteries the cross-section is circular, $\mathcal{I} \equiv \max\{d_2, d_3\}/\min\{d_2, d_3\} \leq 1.2$. The bifurcation cross-section is the first cross-section in the trunk iterations where $\mathcal{I} > 1.9$ and at least one of previous cross-sections have parameter $\mathcal{I} \leq 1.2$. Our criterion for bifurcation intersection is more stable than the criterion proposed in [22].

The application of the Frangi vesselness measure for bifurcation analysis does not provide anatomically correct segmentation of the bifurcation in all cases. We use a 3D Hessian-based filter [23] for the bifurcation analysis and segmentation. The modified vesselness at scale σ is

$$\hat{V}_\sigma = \left(1 - \frac{|\lambda_3| - |\lambda_2|}{|\lambda_2| + |\lambda_3|}\right)\left(\frac{2}{3}\lambda_1 - \lambda_2 - \lambda_3\right)\left(1 - \mathrm{e}^{-(\lambda_1^2+\lambda_2^2+\lambda_3^2)/(2\beta^2)}\right)$$

and the modified multiscale vesselness is

$$\hat{V}_{\mathrm{mult}} = \max_{\sigma_{\min}\leq\sigma\leq\sigma_{\max}} \hat{V}_\sigma \mathrm{e}^{\sigma/2}.$$

It provides the instruments for the bifurcation analysis. Here $\sigma_{\max}$ is the halved maximal diameter of incident vessels, $\sigma_{\min}$ is set less than $\sigma_{\max}/3$, the exponential term normalizes the vessel response peak at all scales. The two next initial seeds are localized on the bifurcation cross-section at two distinct maxima of the modified vesselness $\hat{V}_{\mathrm{mult}}$. The bifurcation is segmented using thresholding of the modified vesselness values. Cholesterol plaques have much higher intensity than inner voxels of vessels, and it is necessary to shade the plaques prior the bifurcation analysis.

Once the centerlines are extracted, the 1D computational graph is generated by automatic postprocessing of the centerlines [4] which completes the construction of the personalized discrete model of coronary arteries.

The examples of extracted centerlines and segmented vascular region are presented in Figs. 3b and 3c, respectively.

1.3 Patient-specific adaptation of reference 3D models

1.3.1 Adaptation of reference full body model

The development of a new personalized segmented model of a whole body from scratch is a very time consuming process. Assuming we already have a segmented model of some individual, we propose methods for patient-oriented adaptation. In contrast to atlas-based segmentation methods, where the segmentation of full body CT/MRI data is obtained from the atlas of presegmented images of other individuals, our approach is based on the assumption, that patient imaging information is limited to only several transverse images.

The most simple approach is the anthropometric rescaling of the model. We split the reference model in several parts, and adjust their height according to the heights of the related parts of the patient. After that we also adjust the width of these parts according to the patient measurements. As a rule, this operation is not sufficient. The patient may have different body constitution: fat/muscle ratio, pathologies, anatomical features, etc.

In this case we propose transformation of the segmented reference model using several control planes and control points. At first, the user selects several control planes, and tries to adapt the reference model in these planes. Model adaptation in the plane is based on piecewise affine mapping defined by the set of control points. The user marks the same set of control points both on the reference image and on the patient image. Then one maps the reference image to the patient image shifting the control points from original positions to the new ones. The control points may represent the anatomical features of the human body. We assume that the anatomical structure of segmented images of the reference model and the patient model is the same whereas the size and the form of the individual tissues may vary.

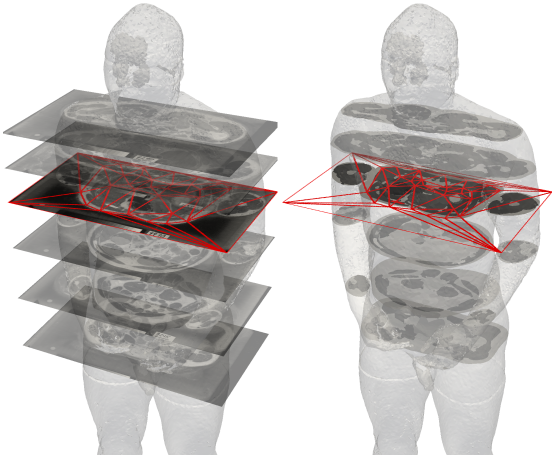

(a)

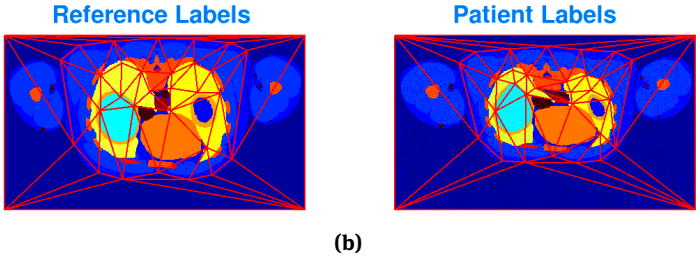

(b)

Figure 4. Piecewise affine mapping of reference model on the left to the patient-specific on the right: (a) 3D mapping reconstructed from several axial control planes, (b) piecewise affine mapping of segmented axial plane and Delaunay triangulation constructed from control points.

The piecewise affine transformation is constructed on the basis of the Delaunay triangulation of the control points from the patient image. The same triangulation with the identical topology is constructed using the corresponding control points in the reference image. Assuming the latter triangulation is not tangled, we can construct the piecewise affine mapping of each triangle from one mesh to the corresponding triangle in the second mesh. Once we constructed the transformations on two parallel control planes, we can define the transformation on any plane between these planes using the linear combination of these two transformations.

An example of 3D transformation based on several control planes is presented in Fig. 4. This transformation was defined by the dozen of axial control planes, only several are presented for visualization purposes. Each plane has a set of control points. These points are placed in the way to transform organs and tissues in thorax region. The detailed algorithm for mapping transformation is presented in [6, 44].

1.3.2 Adaptation of reference vascular network

The reconstruction of entire vascular network on the basis of CT or MRI data is a time consuming procedure. Moreover, only a negligible part of CT/MRI clinical cases provides data for the full body of the patient. The vast majority of CT/MRI clinical cases are focused on detailed individualized analysis of regional or local part of cardiovascular network. Many applications allow to describe the rest of the network in less details.

According to this concept we propose to use anatomically correct data [55] as the reference common structure for all individual cases. The local region of interest is replaced by patient specific CT or MRI data. The reference data can be adapted by the individual data once the respective 1D network structures are recovered in terms of 3D graphs. A 3D graph $T = (V, E)$ is composed by nodes V and edges E sets. Each node attributes coordinates (x, y, z), whereas each edge is presented by a vessel centerline (a sequence of central points and associated vessel mean radii). Basing on anatomical evidence we assume that adaptation of the global reference graph reduces to merging certain nodes of the local patient-specific graph and certain nodes of the global reference graph and eliminating edges of the local reference subgraph.

We developed a black box algorithm for local patient-specific adaptation of the reference vascular network. The algorithm is a specific realization of a general approach whose detailed description and applications are given in [4]. The approach is based on inexact graph matching [25, 29] and considers similarities between geometric and topological features.

Let a global reference graph $T_r = (V_r, E_r)$ and a local patient-specific graph $T_p = (V_p, E_p)$ be given. The global adapted graph $T_{r'}$ is built on the basis of the association set V_{rp} for elements from V_r and V_p. V_{rp} contains pairs of similar nodes from V_r and V_p which are detected by a function f_s, $0 \le f_s \le 1$, specifying similarity between nodes:

$$V_{rp} = \left\{ \{v_r, v_p\} \in V_r \times V_p \mid f_s(v_r, v_p) \ge \Delta \right\} \tag{1.1}$$

where $0.5 \le \Delta \le 0.7$ is a threshold parameter. The closer similarity function f_s is to 1, the stronger similarity between elements v_r, v_p is. In this application we design f_s basing on local properties of branching nodes as follows.

Let E_v denote the set of edges adjacent to the graph node v and $r_v(e)$ is the local radius of the vessel corresponding to edge e near the node v. We define $R_1(v) = \max_{e \in E_v}(r_v(e))$ as the maximal value of $r_v(e)$ for the node v and $R_2(v)$, $R_3(v)$ as the second largest and the third largest values of $r_v(e)$. If the node v has only $0 < k < 3$ adjacent edges then $R_i(v) = 0$ for $i > k$. Our function f_s of similarity between the branching nodes is:

$$f_s(v_r, v_p) = \prod_{i=1}^{3} \left(1 - \frac{|R_i(v_r) - R_i(v_p)|}{\max(R_1(v_r), R_1(v_p))} \right). \tag{1.2}$$

Function f_s measures similarity of two junctions of three vessels associated with the graphs T_r and T_p. Let $E_{\hat{r}}$ be the subset of E_r containing edges on all possible shortest paths in the reference graph T_r between the nodes contributing to V_{rp}, and $V_{\hat{r}}$ be the set of nodes of edges from $E_{\hat{r}}$ not contributing to V_{rp}. To define the global adapted graph $T_{r'} = (V_{r'}, E_{r'})$, we first set $E_{r'} = E_r \setminus E_{\hat{r}}$ and $V_{r'} = V_r \setminus V_{\hat{r}}$, and merge $E_{r'}$ with E_p, and $V_{r'}$

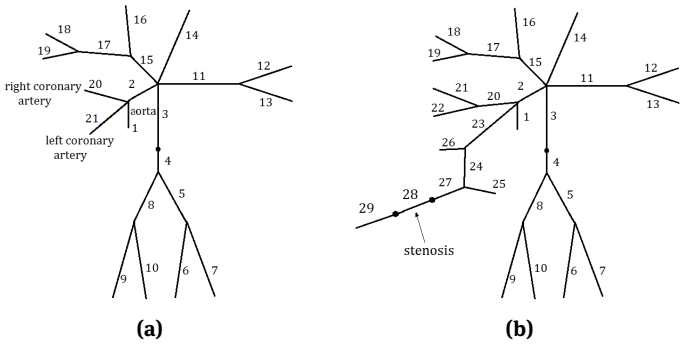

Figure 5. Patient-specific adaptation of a simple reference arterial network: (a) simple reference arterial network with two elementary coronary vessels, (b) adapted arterial network (vessels with indexes more than 19 correspond to patient-specific coronary arteries).

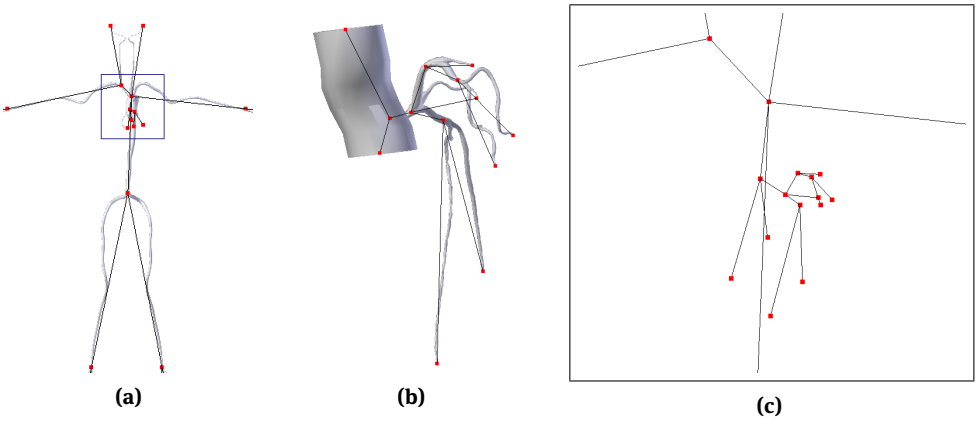

Figure 6. Patient-specific adaptation of a reference arterial network: (a) reference arterial network, (b) individual coronary network, (c) adapted arterial network (zoom).

with V_p. Merging nodes implies that the nodes from V_p not contributing to V_{rp} are added to $V_{r'}$. Merging edges implies that the edges from E_p are added to $E_{r'}$ with simultaneous replacement of the nodes contributing to V_{rp} with their pair associates.

The function f_s does not take into account spatial positions of the reference and the local patient-specific graphs. Therefore, it is applicable for defining association between 3D graphs constructed from different data sets corresponding to the same anatomical regions with anthropometric similarity.

The adaptation of a simple reference arterial network (Fig. 5a) by a patient-specific coronary network (Fig. 2) is shown in Fig.5b. Adaptation of a more complex reference arterial network (Fig. 6a) by a patient-specific coronary network (Fig. 6b) is presented in Fig. 6c. Both reference arterial networks are recovered from geometric 3D data [55] on the basis of algorithm proposed in [12].

2 Applications

2.1 Patient-specific computation of fractional flow reserve

In this section we apply the patient-specific arterial network presented in Fig. 5b to personalized computation of the fractional flow reserve (FFR) at different stenosis degrees by the 1D network blood flow model [39]. Apart of geometric patient-specific data (length and diameter of vessels, individual network structure), the blood

flow model requires elastic properties of the vessels and hydraulic resistance coefficients. Individual elastic properties are beyond the reach of routine examinations, thus we exploit typical values from clinical studies [1, 36] categorized according to age, physical conditions, etc. Hydraulic resistance coefficients are adjusted by fitting model linear velocity to individual ultrasound measurements. The main individual component for patient-specific FFR assessment is the 3D structure of the vascular network which can be recovered from CT/MRI data by the methods discussed in Section 1.2.2.

The model of blood flow in vascular network considers unsteady flows of viscous incompressible fluid in the network of elastic tubes. The model accounts systemic arteries and veins of the reference network. Patient-specific coronary tree is recovered by the methods from section 1.2.2. The model accounts the active vessel wall response (autoregulation) function. Below we outline the basic features of the model, the details can be found in [13, 38, 45].

The flow in every vessel is described by mass and momentum balance equations

$$\partial S_k/\partial t + \partial(S_k u_k)/\partial x = 0 \tag{2.1}$$

$$\partial u_k/\partial t + \partial\left(u_k^2/2 + p_k/\rho\right)/\partial x = f_{fr}\left(S_k/S_k^0, u_k\right), \tag{2.2}$$

where k is the index of the vessel, t is the time, x is the coordinate along the vessel, ρ is the blood density, $S_k(t, x)$ is the vessel cross-section area, S_k^0 is the unstressed vessel cross-section area, p_k is the blood pressure, $u_k(t, x)$ is the linear velocity averaged over the cross-section, f_{fr} is the friction force. The elastic properties of the vessel wall material are incorporated as $p_k(S_k)$ relation

$$p_k(S_k) - p_{\star k} = \rho c_k^2 f(S_k) \tag{2.3}$$

where $f(S_k)$ is a monotone S-like function, $p_{\star k}$ is the pressure in the tissues surrounding the vessel, c_k is small disturbances propagation velocity in the vessel wall.

At the vessels junctions the Poiseuille's pressure drop and mass conservation conditions are applied

$$p_k\left(S_k\left(t, \tilde{x}_k\right)\right) - p_{\text{node}}^l(t) = \varepsilon_k R_k^l S_k\left(t, \tilde{x}_k\right) u_k\left(t, \tilde{x}_k\right), \quad k = k_1, k_2, \ldots, k_M \tag{2.4}$$

$$\sum_{k=k_1,k_2,\ldots,k_M} \varepsilon_k S_k\left(t, \tilde{x}_k\right) u_k\left(t, \tilde{x}_k\right) = 0 \tag{2.5}$$

where M is the number of the connected tubes, $\{k_1, \ldots, k_M\}$ is the range of the indexes of the connected tubes, l is the node index, $p_{node}^l(t)$ is the pressure at the l-th junction point, $\varepsilon = 1$ and $\tilde{x}_k = L_k$ for incoming tubes, $\varepsilon = -1$ and $\tilde{x}_k = 0$ for outgoing tubes, R_k^l is the hydraulic resistance. The set (2.4)–(2.5) is closed by finite differences approximation of compatibility conditions along outgoing characteristics [38].

At the entry point of the vascular network the blood flow is given by the heart ejection

$$u(t, 0)\, S(t, 0) = Q_H(t) \tag{2.6}$$

where function $Q_H(t)$ for normal heart rate (60 beats per minute) is known [14]. We consider different heart rates and scale $Q_H(t)$ so that the volume of blood ejected in one cardiac cycle (stroke volume) remains constant (60 ml), see Fig. 7.

The autoregulation (the adaptation of the vessel wall elasticity to the changes of average flow) introduces essential deviations from the response of passive elastic tubes. In the model we account the autoregulation as dependence of c_k in (2.3) from average pressure $\overline{p}_k$ [38]. The value c_k is updated every heart cycle according to

$$c_k(t) = c_{k,\text{old}} + y\frac{t - T_3}{T_4 - T_3}(c_{k,\text{new}} - c_{k,\text{old}}) \tag{2.7}$$

where

$$c_{k,new} = c_{k,old}\sqrt{\frac{\overline{p}_{k,new}}{\overline{p}_{k,old}}}, \tag{2.8}$$

$$\overline{p}_{k,\text{new}} = \frac{1}{(T_3 - T_2)l_k}\int_{T_2}^{T_3}\int_0^{l_k} p(x, t)\,\mathrm{d}x\,\mathrm{d}t, \qquad \overline{p}_{k,\text{old}} = \frac{1}{(T_2 - T_1)l_k}\int_{T_1}^{T_2}\int_0^{l_k} p(x, t)\,\mathrm{d}x\,\mathrm{d}t$$

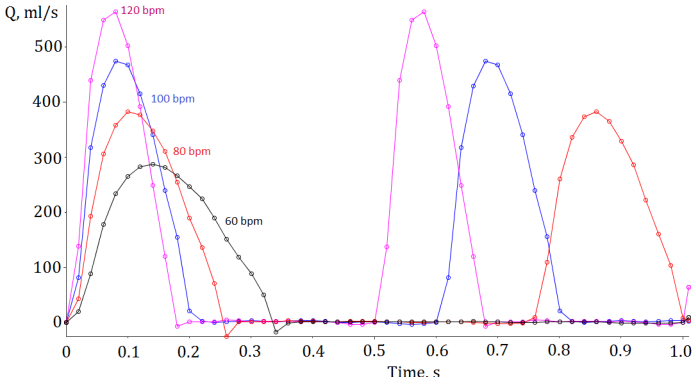

Figure 7. Aortic blood flow time profiles at different heart rates in bpm (beats per minute).

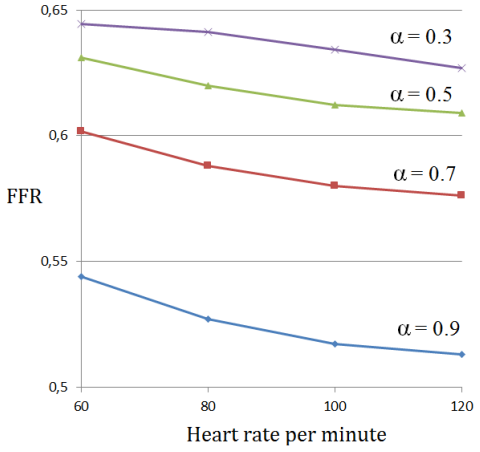

Figure 8. Numerical FFR calculated for selected degrees of stenosis α at different heart rates.

while l_k is the length of k-th vessel; T_1, T_2, T_3, T_4 are the initial moments of the successive cardiac cycles, $0 \leqslant y \leqslant 1$ is the parameter controlling the autoregulation response rate. We associate $y = 1$ with the normal vessel state and $y = 0.1$ with the impact of vasodilator administration.

An additional important feature of coronary haemodynamics is the compression of a part of coronary arteries during diastole when the main myocardial perfusion occurs [37]. We account this feature by setting variable external pressure $p_\star(t) = P_{\text{ext}}^{\text{cor}}(t)$ in (2.3). The shape of the function $P_{\text{ext}}^{\text{cor}}(t)$ is similar to the heart outflow time profile presented in Fig. 7. The peak value is normalized by the ventricular pressures that give 120 mm Hg and 30 mm Hg for branches of left and right coronary artery, respectively [13].

We introduce a stenosis in the model as separate vessel No. 28 (Fig. 5) and compute the FFR as the ratio of average pressure in coronary artery downstream the stenosis (vessel No. 29) to average aortic pressure during vasodilator administration [52]:

$$FFR = \frac{\overline{P}_{29}}{\overline{P}_{\text{aor}}}.$$

To imitate the stenosis as shown in Fig. 5b, we set

$$L_{28} = 0.3 \text{ cm}, \qquad S_{0_{28}} = (1-\alpha)S_{0_{27}}, \qquad R_{28} = \frac{1}{(1-\alpha)^2}\frac{L_{28}}{L_{27}}R_{27}$$

where α is the stenosis fraction, $\alpha = 0.3, 0.5, 0.7, 0.9$. For neighbouring healthy vessels we set $L_{26} = L_{27} = 1.075$ cm, $S_{0_{26}} = S_{0_{27}} = 0.0109$ cm^2, $R_{26} = R_{27} = 7200$ bar/(s $\cdot$ cm^3). Vasodilator administration is imitated by doubling S_0 in all coronary vessels, decreasing resistance R by a factor of 5 and setting $y = 0.1$ in (2.7). For each degree of stenosis and each heart rate profile (Fig. 7) we calculate the FFR on the basis of the numerical pressures. The computed FFR are presented in Fig. 8.

From Fig. 8 we conclude that FFR may depend on the heart rate. In particular, FFR for the patient in quiet conditions with the normal heart rate may overrate FFR at high heart rates, and the larger is the stenosis, the larger overestimation is given at high heart rates. Increased heart rates may occur outside the hospital due to various reasons including psychological stress and physical activity. This risk should be considered by clinicians making decision on invasive (surgical intervention) or non-invasive (therapeutic) stenosis treatment.

Since FFR values for normal and intensive heart rate are different and clinical measurements are available in quiet conditions only, it is important to evaluate individual FFR *in silico*. The presented model and methods of the patient-specific vascular network reconstruction allow to achieve this goal.

2.2 Anatomical models in cardiac electrophysiology

In this section we study the application of anatomical models in cardiac electrophysiology. We couple two electrophysiology mathematical models, and produce the preliminary results of ECG modelling as a proof-of-concept.

There are three commonly used formulations of tissue-level cardiac electrophysiology: the *monodomain* formulation, which provides the trans-membrane voltage V_m throughout the tissue as a function of space and time; the more sophisticated *bidomain* formulation, which provides voltage V_m and extracellular potential φ_e; and bidomain case where an extra-cardiac electrically conductive bath (e.g. torso) is also modelled, which we will refer to as the *bidomain-with-bath* formulation.

The following two bidomain equations are used [24]:

$$\nabla \cdot ((\sigma_i + \sigma_e)\nabla \varphi_e) = -\nabla \cdot (\sigma_i \nabla V_m) + I_{s1} \tag{2.9}$$

$$\nabla \cdot (\sigma_i \nabla V_m) + \nabla \cdot (\sigma_i \nabla \varphi_e) = A_m \left(C_m \frac{\partial V_m}{\partial t} + I_{\text{ion}} \right) - I_{s2} \tag{2.10}$$

where $V_m = \varphi_i - \varphi_e$ is the transmembrane potential, φ_i and φ_e are the intracellular and extracellular electrical potentials, respectively, σ_i and σ_e are the intracellular and extracellular conductivity tensors, respectively, I_{s1} and I_{s2} are the extracellular and intracellular external stimulus currents, respectively, A_m is the surface to volume ratio of the cell membrane, C_m is the membrane capacitance per unit area, and I_{ion} is the sum of all ionic currents calculated from the cellular model.

The extracellular domain is sometimes assumed to be highly conducting ($\sigma_e \sim \infty$) or the domains are assumed to be equally anisotropic ($\sigma_i = \lambda \sigma_e$) in the effort to reduce the bidomain equations to a single equation, hence reducing the amount of computational effort required to solve the problem. The simplified equation is known as the monodomain equation and can be written as

$$\nabla \cdot (\sigma \nabla V_m) = A_m \left(C_m \frac{\partial V_m}{\partial t} + I_{\text{ion}} \right) - I_s \tag{2.11}$$

where the transmembrane potential is equal to the intracellular potential. Here $\sigma = \sigma_i/(1+\lambda)$ and $I_s = I_{s1}/(1+\lambda) + I_{s2}$. We note that the case $\sigma_e \sim \infty$ is equivalent to $\lambda = 0$. In the monodomain formulation we assume no connection between the intracellular domain and any surrounding media, so the following boundary condition is imposed to prevent current flow out of the myocardial domain:

$$(\sigma \nabla V_m) \cdot \mathbf{n} = 0 \tag{2.12}$$

where $\mathbf{n}$ is an external unit normal vector.

The governing equations for the problem of calculating the potential distribution within the torso are the Maxwell's equations. These equations may be simplified by the quasi-static assumption [31]. For the range of frequencies over which bioelectric signals are generated, the capacitive, inductive and propagation effects of the body may be ignored leaving the torso to be modelled as a passive volume conductor. Under these assumptions we reuse our numerical model from [7] for electrical fields distribution during bioimpedance measurements and derive the following Laplace equation:

$$\nabla \cdot (\sigma_o \nabla \varphi_o) = 0 \quad \text{in } T \tag{2.13}$$

with the boundary conditions

$$\sigma_o \nabla \varphi_o \cdot \mathbf{n} = 0 \quad \text{on } \partial T \backslash \Gamma_H \tag{2.14}$$

$$\varphi_o = V_m \quad \text{on } \Gamma_H \tag{2.15}$$

where T is the extracardiac part of the human torso (computational domain), ∂T is its boundary, Γ_H is the heart-torso interface, $\mathbf{n}$ is the external unit normal vector for T, φ_o is the electric potential, σ_o is the conductivity tensor. Equation (2.13) determines the distribution of electric field in the domain with heterogeneous conductivity σ_o. Equation (2.14) defines the no-flow condition on the external boundary. The use of Dirichlet boundary conditions on Γ_H (2.15) decouples equations in the heart and T. Coupled equations (2.9)–(2.10) and (2.13)-(2.14) imply the continuity of both current density and extracellular potential on the surface Γ_H and constitute the bidomain-with-bath model.

In the current work we use the monodomain cardiac equation and the Laplace equation in torso. The accuracy of the results depends on two factors: the actual coupling/decoupling technique used and the type of potential continuity $\varphi_o = \varphi_e$ or $\varphi_o = V_m$. The simplified condition (2.15) provides only qualitative but not quantitative results. In future work we will use more accurate bidomain-with-bath model. The monodomain simulation is performed with the open source simulation package Chaste [26, 30]. The P1 finite element discretization of equations (2.13)–(2.14) on unstructured tetrahedral meshes is performed with the open source package Ani3D [54]. In our study we assume that the electrical current does not flow from the heart to the torso, i.e. that the heart is isolated from the torso. This approximation decouples the Laplace equation in the torso from the monodomain equation in the heart, which allows reducing the size of the linear systems to be solved.

The anatomical model of the heart used for this study is a publicly available human ventricular tetrahedral mesh derived from CT data [2]. For reference heart models myocardial fibers orientation can be computed algorithmically [32, 40] and used as anisotropy source in cardiac electrophysiological models. We note that the patient-specific ventricular mesh may be constructed from segmented ventricular images, and the patient-specific fibre orientation may be obtained from MR-DTI imaging [18].

In the absence of the Purkinje network, a time-dependent initial stimulus was applied on the endocardium to mimic a realistic electrical activation sequence in the heart. The duration of the intra-cellular stimulus was 2 ms, and its strength was 80 mA cm^{-3}. The membrane parameters are $A_m = 1400\ \text{cm}^{-1}$ and $C_m = 1\ \mu\text{F cm}^{-2}$, the Luo–Rudy cardiac cell model was used. The anisotropic conductivity parameters are $\sigma = 1.75$ mS cm^{-1} in fibre direction and $\sigma = 0.19$ mS cm^{-1} in the transverse and normal directions [3, 43].

The distribution of transmembrane voltage V_m is obtained at time step $t = 50$ ms after heart excitement and it is used as the boundary condition to the Laplace equation. Since the monodomain and the Laplace computational meshes do not match on the surface Γ_H, the piecewise linear interpolation is used to transfer numerical solution from cardiac mesh to the full body mesh. The conductivity tensor in the torso is assumed isotropic. The range of frequencies over which bioelectric signals are generated is low, thus we select conductivity parameters at 10 Hz frequency from the database of dielectric properties of human tissues [11].

In our ECG modelling scenario we examine the impact of the anatomical structure in the thorax region to ECG readings. We used the same computational cardiac mesh and cardiac electrophysiological parameters, and we used two different torso models: the original VHP model and the modified model from Section 1.3.1 (see Fig. 4). The computed surface potential fields are presented in Fig. 9, where one can observe high sensitivity of ECG signals to the position of the heart as well as to the anatomical structure of surrounding tissues. In the modified anatomical model the distance from heart to the body surface is almost twice shorter, and thus maximum potential value on the surface is bigger.

These preliminary results indicate importance of accurate individual thorax reconstruction. The patient-specific segmentation for ECG modelling should be focused on cardiac and surrounding tissues. Although the decoupling approach proposed above is very appealing in terms of the computational cost, additional numerical studies are needed to verify and refine of ECG signals modelling and adopt the coupled bidomain-with-bath electrophysiological problem.

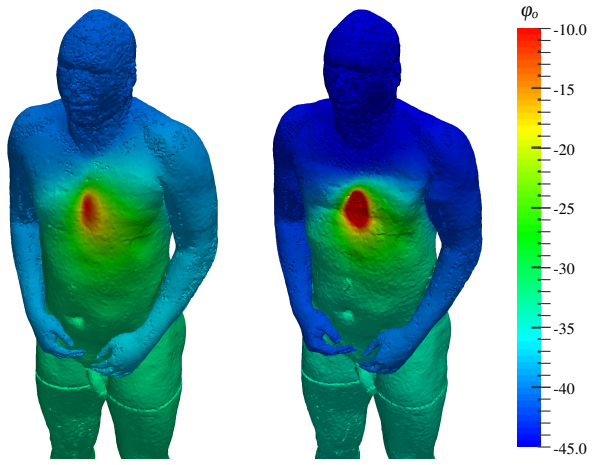

Figure 9. Qualitative comparison of surface electrical potential field φ_o at time 50ms from excitation for different anatomical models: (a) reference anatomical model, (b) modified anatomical model. The legend is given in arbitrary units.

3 Conclusions

We presented our approach to patient-specific simulation of human physiological processes. The foundation of the approach is formed by the set of the methods for individualized 3D reconstruction of body anatomical components on the basis of the medical images and the algorithms for generation of discrete patient-specific anatomical models represented by computational meshes or graphs. Applicability of the approach is presented for the first stage solutions of two medical challenges, the computational evaluation of the fractional flow reserve in coronary arteries and the computer simulations of electrocardiographic measurements.

Acknowledgment: The authors acknowledge the staff of I. M. Sechenov First Moscow State Medical University and especially to P. Kopylov, N. Gagarina, E. Fominykh, A. Dzyundzya for patient-specific data.

Funding: The research was supported by Russian Science Foundation (RSCF) grant 14-31-00024. The second author acknowledges Russian Federation President Grant for Government Support of Young Russian Scientists MK–7839.2015.1 for support of ECG modelling.

References

[1] J. Aguado-Sierra, K. H. Parker, J. E. Davies, D. Francis, A. D. Hughes, and J. Mayer, Arterial pulse wave velocity in coronary arteries. In: *Engineering in Medicine and Biology Society, 2006. EMBS'06. 28th Annual International Conference of the IEEE*. 2006, pp. 867–870.

[2] M. O. Bernabeu, M. Wallman, and B. Rodriguez, Shock-induced arrhythmogenesis in the human heart: A computational modelling study. In: *2010 Annual International Conference of the IEEE Engineering in Medicine and Biology*. 2010, pp. 760–763.

[3] L. Clerc, Directional differences of impulse spread in trabecular muscle from mammalian heart. *J. Physiology* **255** (1976), 335–346.

[4] A. Danilov, Y. Ivanov, R. Pryamonosov, and Y. Vassilevski, Methods of graph network reconstruction in personalized medicine. *Int. J. Numer. Meth. Biomed. Engrg.* (2015) (submitted).

[5] A. A. Danilov, Unstructured tetrahedral mesh generation technology. *Comp. Math. Math. Physics* **50** (2010), 139–156.

[6] A. A. Danilov, V. K. Kramarenko, D. V. Nikolaev, and A. S. Yurova, Personalized model adaptation for bioimpedance measurements optimization. *Russ. J. Numer. Anal. Math. Modelling* **28** (2013), 459–470.

[7] A. A. Danilov, D. V. Nikolaev, S. G. Rudnev, V. Y. Salamatova, and Y. V. Vassilevski, Modelling of bioimpedance measurements: unstructured mesh application to real human anatomy. *Russ. J. Numer. Anal. Math. Modelling* **27** (2012), 431–440.
[8] L. M. Florack, B. M. ter Haar Romeny, J. J. Koenderink, and M. A. Viergever, Scale and the differential structure of images. *Image and Vision Computing* **10** (1992), 376–388.
[9] A. Frangi, W. Niessen, K. Vincken, and M. Viergever, Multiscale vessel enhancement filtering. In: *Medical Image Computing and Computer-Assisted Interventation – MICCAI'98*. 1998, pp. 130–137.
[10] P. J. Frey and P.-L. George. *Mesh generation: application to finite elements*. Hermes Science, Paris, Oxford, 2000.
[11] S. Gabriel, R. W. Lau, and C. Gabriel, The dielectric properties of biological tissues: II. Measurements in the frequency range 10 Hz to 20 GHz. *Phys. Med. Biology* **41** (1996), 2251–2269.
[12] T. Gamilov, Y. Ivanov, P. Kopylov, S. Simakov, and Y. Vassilevski, Patient specific haemodynamic modelling after occlusion treatment in leg. *Math. Modelling Natur. Phenom.* **9** (2014), 85–97.
[13] T. M. Gamilov and S. S. Simakov, Modelling of coronary flow stimulation by enhanced external counterpulsation. *Int. J. Numer. Meth. Biomed. Engrg.* (2015) (submitted).
[14] W. Ganong. *Review of Medical Physiology*. Appleton & Lange, Stamford, CT, 1999.
[15] L. Grady, Fast, quality, segmentation of large volumes – Isoperimetric distance trees. In: *Computer Vision – ECCV 2006*. 2006, pp. 449–462.
[16] K. H. Höhne, B. Pflesser, A. Pommert, M. Riemer, R. Schubert, T. Schiemann, U. Tiede, U. Schumacher, et al., A realistic model of human structure from the Visible Human data. *Meth. Inform. Medicine* **40** (2001), 83–89.
[17] M. Holtzman-Gazit, R. Kimmel, N. Peled, and D. Goldsher, Segmentation of thin structures in volumetric medical images. *IEEE Trans. Image Processing* **15** (2006), 354–363.
[18] E. W. Hsu, L. J. Healy, D. R. Einstein, and A. P. Kuprat, Imaging-based assessment and modelling of the structures of the myocardium. In: *Computational Cardiovascular Mechanics*. 2009, pp. 23–39.
[19] J. Kellett and S. Rasool, The prediction of the in-hospital mortality of acutely ill medical patients by electrocardiogram (ECG) dispersion mapping compared with established risk factors and predictive scores – A pilot study. *Europ. J. Intern. Medicine* **22** (2011), 394–398.
[20] F. Kopylov, A. Bykova, Y. Vassilevski, and S. Simakov, The role of fractional flow reserve estimate in coronary arteries atherosclerosis. *Therapeutic archive* (2015) (to appear).
[21] S. Krishnamoorthi, L. E. Perotti, N. P. Borgstrom, O. A. Ajijola, A. Frid, A. V. Ponnaluri, J. N. Weiss, Z. Qu, W. S. Klug, D. B. Ennis, and A. Garfinkel, Simulation methods and validation criteria for modelling cardiac ventricular electrophysiology. *PLoS ONE* **9** (2014), e114494.
[22] R. P. Kumar, F. Albregtsen, M. Reimers, B. Edwin, T. Langø, and O. J. Elle, Blood vessel segmentation and centerline tracking using local structure analysis. In: *IFMBE Proceedings*. 2015, pp. 122–125.
[23] R. P. Kumar, F. Albregtsen, M. Reimers, T. Langø, B. Edwin, and O. J. Elle, 3D multiscale vessel enhancement based centerline extraction of blood vessels. In: *Medical Imaging 2013: Image Processing*. 2013, doi: 10.1117/12.2006779.
[24] G. Lines, M. Buist, P. Grottum, A. Pullan, J. Sundnes, and A. Tveito, Mathematical models and numerical methods for the forward problem in cardiac electrophysiology. *Comput. Visual. Sci.* **5** (2002), 215–239.
[25] J. H. Metzen, T. Kröger, A. Schenk, S. Zidowitz, H.-O. Peitgen, and X. Jiang, Matching of anatomical tree structures for registration of medical images. *Image Vision Comp.* **27** (2009), 923–933.
[26] G. R. Mirams, C. J. Arthurs, M. O. Bernabeu, R. Bordas, J. Cooper, A. Corrias, Y. Davit, S.-J. Dunn, A. G. Fletcher, D. G. Harvey, M. E. Marsh, J. M. Osborne, P. Pathmanathan, J. Pitt-Francis, J. Southern, N. Zemzemi, and D. J. Gavaghan, Chaste: An open source C++ library for computational physiology and biology. *PLoS Computational Biology* **9** (2013), e1002970.
[27] P. D. Morris, D. Ryan, A. C. Morton, R. Lycett, P. V. Lawford, D. R. Hose, and J. P. Gunn, Virtual fractional flow reserve from coronary angiography: Modelling the significance of coronary lesions. *JACC: Cardiovasc. Interventions* **6** (2013), 149–157.
[28] P. Pathmanathan and R. A. Gray, Verification of computational models of cardiac electro-physiology. *Int. J. Numer. Meth. Biomed. Engrg.* **30** (2013), 525–544.
[29] M. Pelillo, K. Siddiqi, and S. Zucker, Matching hierarchical structures using association graphs. *IEEE Trans. Pattern Anal. Mach. Intelligence* **21** (1999), 1105–1120.
[30] J. Pitt-Francis, P. Pathmanathan, M. O. Bernabeu, R. Bordas, J. Cooper, A. G. Fletcher, G. R. Mirams, P. Murray, J. M. Osborne, A. Walter, S. J. Chapman, A. Garny, I. M. van Leeuwen, P. K. Maini, B. Rodríguez, S. L. Waters, J. P. Whiteley, H. M. Byrne, and D. J. Gavaghan, Chaste: A test-driven approach to software development for biological modelling. *Comp. Phys. Commun.* **180** (2009), 2452–2471.
[31] R. Plonsey and D. Fleming. *Bioelectric Phenomena*. McGraw-Hill, New York, 1969.
[32] M. Potse, B. Dube, J. Richer, A. Vinet, and R. Gulrajani, A comparison of monodomain and bidomain reaction-diffusion models for action potential propagation in the human heart. *IEEE Trans. Biomed. Engrg.* **53** (2006), 2425–2435.
[33] A. G. Radaelli and J. Peiró, On the segmentation of vascular geometries from medical images. *Int. J. Numer. Meth. Biomed. Engrg.* **26** (2010), 3–34.
[34] R. Rajani, Y. Wang, A. Uss, D. Perera, S. Redwood, M. Thomas, J. B. Chambers, R. Preston, G. S. Carr-White, and P. Liatsis, Virtual fractional flow reserve by coronary computed tomography – hope or hype? *EuroIntervention* **9** (2013), 277–284.
[35] L. Rineau and M. Yvinec, A generic software design for Delaunay refinement meshing. *Comput. Geometry* **38** (2007), 100–110.

[36] E. R. Sala, J. C. Rosell, C. P. Encinas, J. C. Muñoz, F. P. Lahiguera, J. C. Alós, K. Herzig, and J. M. P. Izuel, The continuum of pulse wave velocity from young elite athletes to uncontrolled older patients with resistant hypertension. *J. Hypertension* **28** (2010), e313, pp.19.216.
[37] R. F. Schmidt and G. Thews. *Human Physiology*. Springer-Verlag, Berlin, Heidelberg, 1989.
[38] S. S. Simakov, T. M. Gamilov, and Y. N. Soe, Computational study of blood flow in lower extremities under intense physical load. *Russ. J. Numer. Anal. Math. Modelling* **28** (2013), 485–504.
[39] S. S. Simakov and A. S. Kholodov, Computational study of oxygen concentration in human blood under low frequency disturbances. *Math. Models Comput. Simul.* **1** (2009), 283–295.
[40] D. D. Streeter, H. M. Spotnitz, D. P. Patel, J. Ross, and E. H. Sonnenblick, Fiber orientation in the canine left ventricle during diastole and systole. *Circul. Research* **24** (1969), 339–347.
[41] G. Taubin, A signal processing approach to fair surface design. In: *Proceedings of the 22nd annual conference on Computer Graphics and Interactive Techniques – SIGGRAPH'95*. 1995, pp. 351–358.
[42] H. Tek, M. A. Gulsun, S. Laguitton, L. Grady, D. Lesage, and G. Funka-Lea, Automatic coronary tree modelling. *The Midas Journal – 2008 MICCAI Workshop Grand Challenge Coronary Artery Tracking* (2008) http://hdl.handle.net/10380/1426.
[43] N. Trayanova, J. Eason, and F. Aguel, Computer simulations of cardiac defibrillation: a look inside the heart. *Comput. Visual. Sci.* **4** (2002), 259–270.
[44] Y. Vassilevski, A. Danilov, Y. Ivanov, S. Simakov, and T. Gamilov, Personalized anatomical meshing of the human body with applications. In: *Modelling the Heart and the Circulatory System*. 2015, pp. 221–236.
[45] Y. Vassilevski, S. Simakov, V. Salamatova, Y. Ivanov, and T. Dobroserdova, Numerical issues of modelling blood flow in networks of vessels with pathologies. *Russ. J. Numer. Anal. Math. Modelling* **26** (2012), 605–622.
[46] Y. V. Vassilevski, A. V. Vershinin, A. A. Danilov, and A. V. Plenkin, Tetrahedral mesh generation in domains defined in CAD systems. In: *Matrix Methods and Techniques for Solving Large Problems*. 2005, pp. 21–32, (in Russian).
[47] Z. Wu and J. M. Sullivan, Multiple material marching cubes algorithm. *Int. J. Numer. Meth. Engrg.* **58** (2003), 189–207.
[48] G. Yang, P. Kitslaar, M. Frenay, A. Broersen, M. J. Boogers, J. J. Bax, J. H. C. Reiber, and J. Dijkstra, Automatic centerline extraction of coronary arteries in coronary computed tomographic angiography. *Int. J. Cardiovasc. Imaging* **28** (2012), 921–933.
[49] S. Y. Yeo, X. Xie, I. Sazonov, and P. Nithiarasu, Segmentation of biomedical images using active contour model with robust image feature and shape prior. *Int. J. Numer. Meth. Biomed. Engrg.* **30** (2014), 232–248.
[50] Y. E. Yoon and B.-K. Koo, Non-invasive functional assessment using computed tomography: When will they be ready for clinical use? *Cardiovasc. Diagnosis Therapy* **2** (2012), 106–112.
[51] P. A. Yushkevich, J. Piven, H. C. Hazlett, R. G. Smith, S. Ho, J. C. Gee, and G. Gerig, User-guided 3D active contour segmentation of anatomical structures: Significantly improved efficiency and reliability. *NeuroImage* **31** (2006), 1116–1128.
[52] C. K. Zarins, C. A. Taylor, and J. K. Min, Computed fractional flow reserve (FFTCT) derived from coronary CT angiography. *J. Cardiovasc. Transl. Research* **6** (2013), 708–714.
[53] N. Zemzemi, M. O. Bernabeu, J. Saiz, J. Cooper, P. Pathmanathan, G. R. Mirams, J. Pitt-Francis, and B. Rodriguez, Computational assessment of drug-induced effects on the electrocardiogram: from ion channel to body surface potentials. *British J. Pharmacol.* **168** (2013), 718–733.
[54] Advanced Numerical Instruments 3D, http://sourceforge.net/projects/ani3d.
[55] Anatomy 3D Models – Plasticboy, http://www.plasticboy.co.uk/store/.
[56] The National Library of Medicine's Visible Human Project, http://www.nlm.nih.gov/research/visible.